UAB

Universitat Autònoma de Barcelona

Departament de Química

Facultat de Ciències

New Functional Ligands for the Preparation of Photoactive Nanoparticle-Based Materials

Laura Amorín Ferré

Ph.D. Thesis

Ph.D. in Chemistry

2014

Supervisors:

Dr. José Luis Bourdelande Fernández

Dr. Félix Busqué Sánchez

Dr. Jordi Hernando Campos

IV.2.2.1. Synthesis of quantum dots

As earlier described, both pure core CdSe and core/shell CdSe/ZnS QDs were synthesized and used in this work to undertake for the first time the preparation of discrete, covalently-tethered QD heteroaggregates. In all cases, commercially available OA was used as organic stabilizer for the synthesis of the nanocrystals, since preliminary experiments conducted in our group by Dr. Enrico Faggi demonstrated that (i) more stable QDs were obtained, and (ii) this allowed for simpler ligand exchange processes than when using other type of capping layers such as trioctylphosphine oxide. Thus, OA-coated CdSe QDs were prepared using the procedure described by Yu *et al.* (Scheme IV-18).[45] As discussed in the introduction of this chapter, this method relies on the formation of oleate cadmium salts in the reaction medium, which, after the addition of TOPSe at high temperature, leads to the nucleation and growth of the QDs.
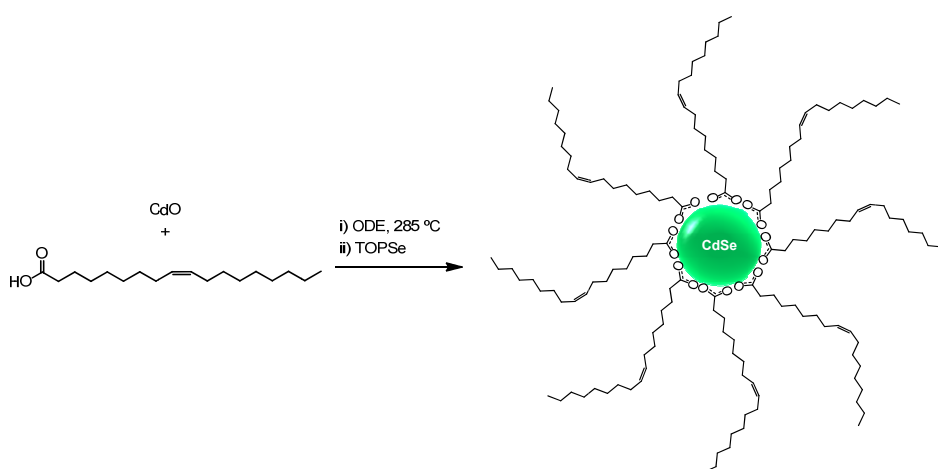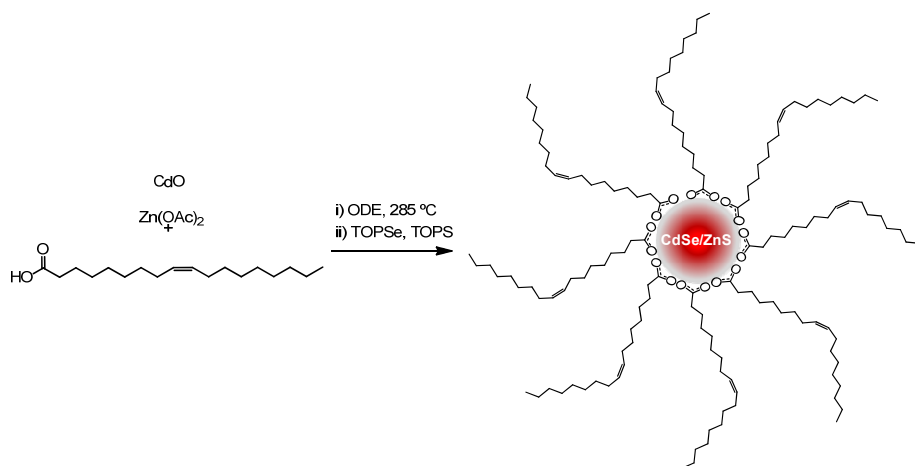

Scheme IV-18. Representative reaction conditions used for the formation of pure core CdSe QDs.

Reaction time at high temperature is a key parameter in this synthetic methodology, because it determines the growth time of the QDs and, therefore, their final size and optical properties. Thus, the absorption and emission spectra of the resulting nanocrystals could by finely tuned by accurately controlling this parameter, as demonstrated in Figure IV-15. Clearly, longer reaction times resulted in larger QD sizes and smaller HOMO-LUMO gaps. As a consequence, CdSe QDs with rationally designed optical properties could be easily prepared on demand.
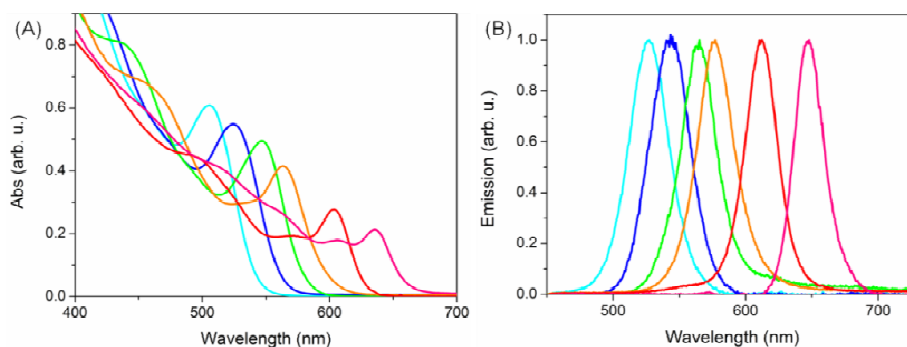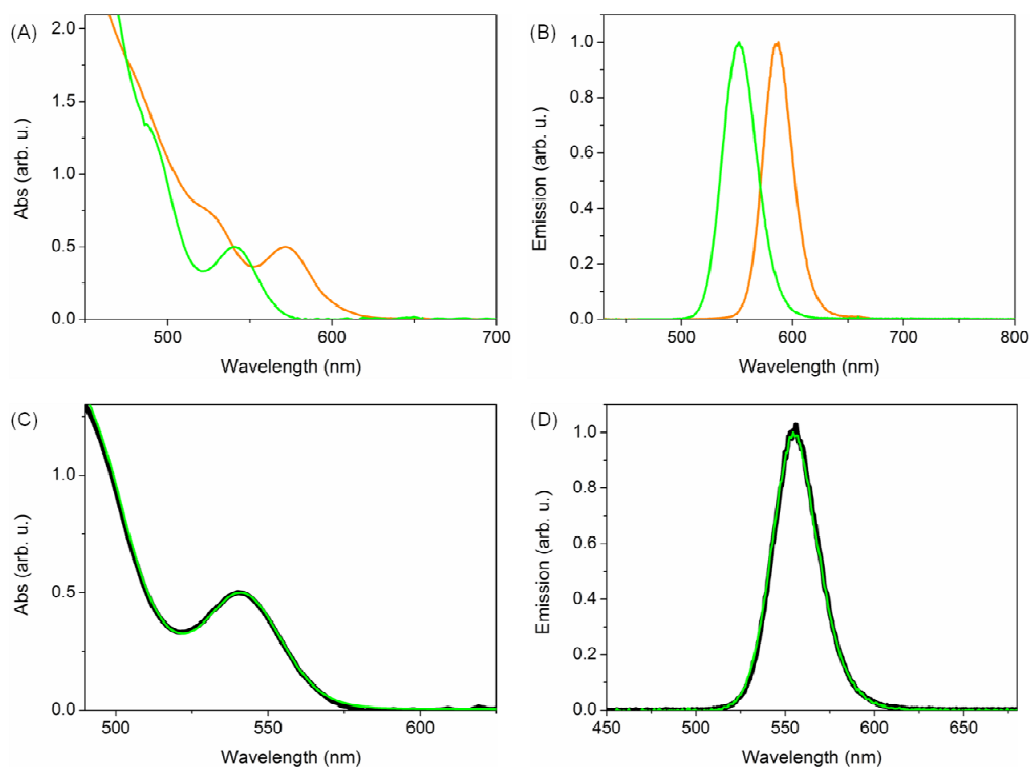

Figure IV-15. (A) Absorption and (B) emission spectra of different pure core CdSe QDs synthesized in this work. From high to low optical bandgaps, the following reaction times were used: 5 s, 10 s, 1 min, 5 min, 10 min and 30 min.

CdSe/ZnS QDs were synthesized by means of the simple, one-pot strategy reported by Bae *et al.*[9] This method consists in the rapid injection of a previosly prepared solution of TOPSe and TOPS to a hot mixture of Cd(oleate) and Zn(oleate) in ODE, which results in the formation of composition gradient nanocrystals with CdSe-enriched cores and ZnS-enriched shells (Scheme IV-19). After cooling down, the synthesized core/shell QDs were precipitated with an excess of methanol and centrifuged.

Scheme IV-19. Representative reaction conditions used for the preparation of composition gradient $Cd_xSe_y/Zn1_{-x}S_{1-y}$ QDs.

In contrast to pure CdSe QDs and regular CdSe/ZnS QDs prepared by stepwise growth of their core and shells, the HOMO-LUMO gap of composition gradient CdSe/ZnS does not depend on the reaction time for the synthesis of the CdSe core, but on their composition (i.e. the amount of Cd, Zn, Se an S precursors mixed). As earlier commented, this is due to the particular mechanism of formation of these nanocrystals, which relies on the faster nucleation rate of CdSe with respect to ZnS. Therefore, composition must be careful controlled to obtain CdSe/ZnS QDs with the desired optical properties. On the other hand, reaction time controls the thickness of the ZnS shell together with composition. This is clearly illustrated by Figure IV-16, which shows how the absorption and emission spectra of composition gradient CdSe/ZnS nanocrystals vary when tuning these two experimental parameters. For instance, when using equivalent reaction times for the synthesis of CdSe/ZnS QDs but increasing the Se/(Se+Zn) ratio, QDs of similar size but narrower HOMO-LUMO gap were obtained (i.e. larger CdSe core and thinner ZnS shell, Figure IV-16A-B). Instead, by preserving the composition of the precursor mixture but increasing the reaction time, larger QDs with equivalent bandgap were prepared (i.e. similar CdSe core and thicker ZnS shell, Figure IV-16C-D).

Figure IV-16. (A) Absorption and (B) emission spectra of core/shell QDs synthesized with different chemical composition and same reaction times: $Cd_{0.4}Zn_4Se_{0.043}S_{4.3}$, ø = 6.32 ± 0.91 nm (green) and $Cd_{0.4}Zn_{4.1}Se_{0.2}S_{4.2}$, ø = 6.10 ± 0.66 nm (orange). (C) Absorption and (D) emission spectra of core/shell QDs synthesized with equal chemical composition but different reaction times: $Cd_{0.4}Zn_4Se_{0.043}S_{4.3}$, ø = 6.32 ± 0.91 nm (black) and ø = 9.65 ± 0.85 nm (green).

Once synthesized, both CdSe and CdSe/ZnS QDs were subjected to the same type of purification processes, which were aimed to remove all reaction by-products as well as excess amounts of precursors and oleic acid stabilizers. This was achieved by several redispersion-centrifugation cycles using proper solvents. In particular, special care was taken to wash all QDs of interest until no free OA molecules were observed. We monitored this process by ^{1}H NMR, which allows discriminating between free and QD-tethered organic moieties. This is due to the effect of the metals in the nanocrystals on the relaxation processes of the excited spin states of close-by nuclei, which are dramatically accelerated.[46,47] As such, the linewidths of the corresponding NMR signals are largely increased and, therefore, they significantly broaden. Figure IV-17 nicely demonstrates this effect by comparing the ^{1}H NMR spectrum of oleic acid with those registered during the purification process of OA-coated CdSe/ZnS QDs. While well-resolved ^{1}H NMR multiplets are observed for the QD-free sample of oleic acid, overlapped narrow and broad signals were found in the spectrum of the initial precipitated mixture of nanocrystals, which can be ascribed to the mixture of free and bound OA molecules, respectively.[48] For instance, this is clearly appreciated for the olefinic signals at 5.3-5.4 ppm. As expected, subsequent washing steps of the QD sample resulted in the loss of the narrow signals, thus demonstrating the removal of free oleic acid ligands. Noticeably, some of the signals arising from QD-tethered oleic acid molecules also disappeared in the spectra of the washed samples and no peaks were eventually found in the corresponding

spectral regions (e.g. signals at 2.35 and 1.63 ppm corresponding to H-2 and H-3 located at α- and β-position with respect to the carboxylic group).[46b,49] It must be noted that these are the closest protons to the nanocrystal surface, and therefore, for which the metal-induced effect on spin relaxation should be more pronounced. As a result, their signals become so broad that they can no longer be distinguished from the background.
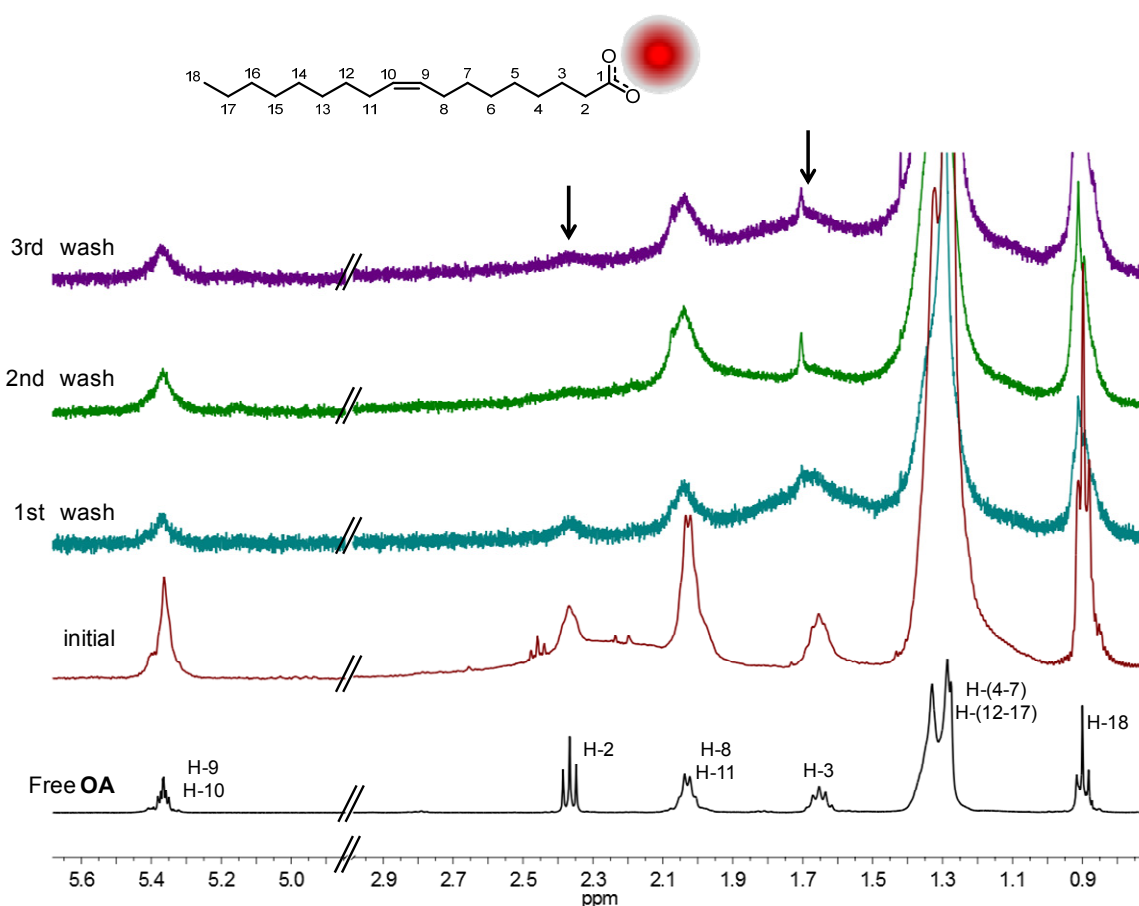
Figure IV-17. ^{1}H NMR (CDCl$_3$, 400 MHz) spectra of free oleic acid (black), the initial reaction mixture of CdSe/ZnS QDs (red) and the consecutive washes done for its purification. Arrows highlight the decrease of the proton signals of the protons closest to the metal surface.

To have a better insight into the effect of QDs on the NMR signals of the bound organic stabilizers, 1D diffusion NMR experiments (1D DOSY NMR) were additionally performed. DOSY NMR is a very powerful spectroscopic technique that allows separate detection of molecules based on their diffusion coefficients and, therefore, their molecular weigh, upon application of a magnetic gradient within the sample.[47] Consequently, it can be used to selectively register the ^{1}H NMR spectrum of the organic ligands tethered to the surface of QDs by setting an appropriate threshold to discriminate between their diffusion coefficients and those of the free, unbound molecules.[50] As a proof of concept, Figure IV-18 plots the 1D DOSY ^{1}H NMR spectrum of the reaction mixture of the same OA-coated CdSe/ZnS shown in Figure IV-17, which is compared to that of free oleic acid. Clearly, the same spectral features observed by regular ^{1}H NMR upon repetitive washing steps (i.e.

broadening and even disappearance of QD-bound OA signals) are directly revealed in this case by DOSY NMR experiments without the need for extensive QD purification.

1D diffusion NMR experiment

QD

^{1}H NMR experiment

OA
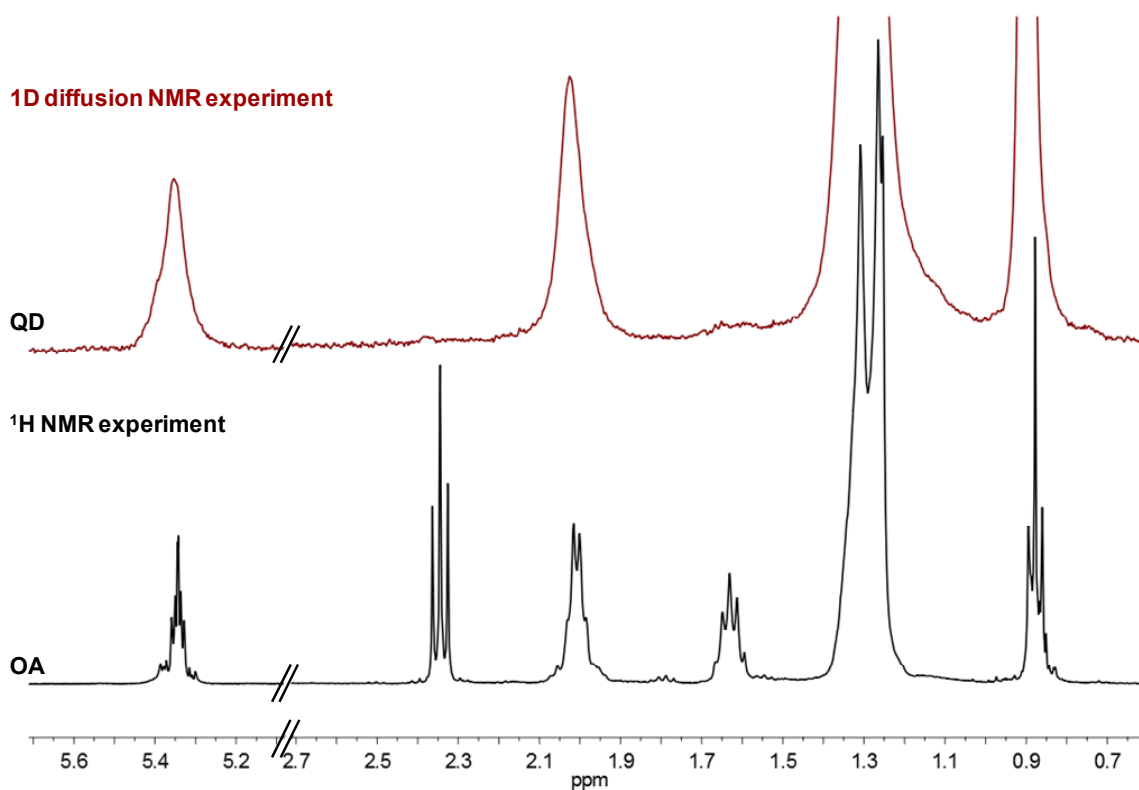
Figure IV-18. Comparison between the 1D DOSY NMR spectrum (CDCl$_3$, 400 MHz) of non-washed OA-coated core/shell CdSe/ZnS QDs and free OA ^{1}H NMR spectrum.

Among all OA-coated QDs synthesized and purified in this work, only four of them were selected to conduct further experiments of ligand exchange and SPAAC-induced heteroaggregation. Three of these QDs were core/shell CdSe/ZnS nanocrystals (**QD1$_{OA}$-QD3$_{OA}$**) of different composition and sizes and, thus, distinct optical properties. The fourth was a pure core CdSe QD (**QD4$_{OA}$**). Table IV-2 summarizes the experimental conditions used for the preparation of these QDs as well as their main morphological and optical properties. In addition, Figure IV-19 shows representative TEM images of these nanocrystals and size distribution histograms, while Figure IV-20 plots their absorption and luminescence spectra.

Table IV-2. Summary of the synthetic experimental conditions and properties of the OA-coated QDs selected for ligand exchange and heteroaggregate formation experiments.
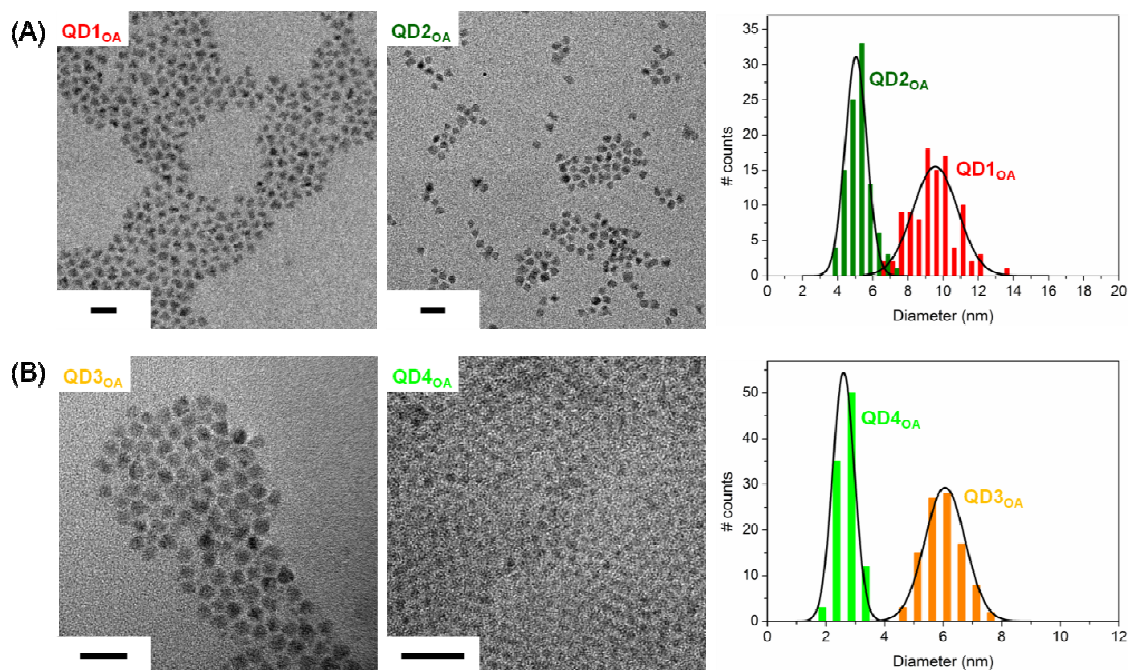
	QD1$_{OA}$	QD2$_{OA}$	QD3$_{OA}$	QD4$_{OA}$
mmol Cd	0.4	0.4	0.4	1
mmol Se	0.4	0.061	0.2	1
mmol Zn	4.0	4.0	4.4	-
mmol S	3.96	4.34	4.2	-
Reaction time	10 min	10 s	10 s	20 s
Diameter (nm)[a]	9.54 ± 1.31	6.32 ± 0.91	6.10 ± 0.66	2.48 ± 0.32
$\lambda_{max,Abs}$ (nm)	609	540	571	525
$\lambda_{max,Em}$ (nm)	623	550	593	532
Diamenter core (nm)[b]	4.65	2.87	3.60	2.52
Shell thickness (nm)	2.44	1.72	1.25	-
PLQY[c]	0.25	0.26	0.26	0.09

[a]Determined by statistical analysis of TEM images (n = 100, errors are standard deviations of the mean). [b]Calculated from Equation IV-1, as described in the text. [c]Determined in CHCl$_3$ using PDI (Φ_{fl} = 1)[51] and PTDCI (Φ_{fl} = 1)[52] as references.

All four QDs selected show narrow emission spectra, which confirm size homogeneity, as proven by the size distribution histograms in Figure IV-19. These histograms clearly illustrate that **QD1$_{OA}$**-**QD3$_{OA}$** present greater dimensions than **QD4$_{OA}$**, which must be ascribed to (i) the presence of the surrounding ZnS shell, and (ii) the larger diameter of their CdSe cores, as demonstrated by their more red-shifted emissions (i.e. smaller HOMO-LUMO gaps). A fair estimation of the core sizes of **QD1$_{OA}$**-**QD3$_{OA}$** can be obtained by Equation IV-1 reported by Yu *et al.*,[53] where D is the estimated diameter core and λ is the first absorption peak in nm.

$$D = (1.6122\cdot10^{-9})\lambda^4 - (2.6575\cdot10^{-6})\lambda^3 + (1.6242\cdot10^{-3})\lambda^2 - 0.4277\lambda + 41.57 \qquad \text{(IV-1)}$$

While the large reaction time required to prepare red-emitting **QD1$_{OA}$** accounts for its large core and shell dimensions, it must be noted that **QD2$_{OA}$** and **QD3$_{OA}$** were obtained with equivalent reaction times. In this case, the differences in CdSe core size and, therefore, HOMO-LUMO gaps arise from the distinct compositions used. As reported by Bae *et al.*[9] and previously discussed, increasing the Se/(Se+Zn) ratio leads to larger CdSe cores and, consequently, red-shifted absorption and emission spectra (Figure IV-20). An additional difference between pure core and core/shell QDs is clearly shown in their absorption spectra (Figure IV-20A). Pure core **QD4$_{OA}$** presents well-defined absorption bands, whereas they are much more diffuse for **QD1$_{OA}$**-**QD3$_{OA}$** due to the composition gradient of their shell.

Figure IV-19. TEM images and histograms of (A) **QD1$_{OA}$** and **QD2$_{OA}$** and (B) **QD3$_{OA}$** and **QD4$_{OA}$**. Scale bars for TEM images are 20 nm.
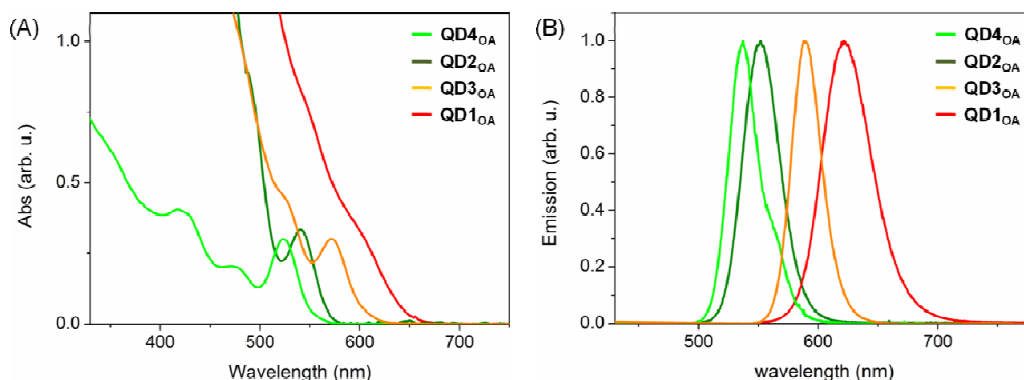
Figure IV-20. (A) Absorption and (B) emission spectra of **QD1$_{OA}$** -**QD4$_{OA}$**.

As further discussed in next section, the PLQY of pure core CdSe QDs is expected to be very sensitive to manipulation, and excessive washings/dilution must result in a decrease in emission intensity from the nanocrystals. Therefore, core/shell QDs are normally preferred for many applications based on their superior brightness and stability. Unfortunately, the presence of the optically inactive ZnS shell in those nanocrystals might be a hurdle for efficient energy transfer between their CdSe cores in QD heteroaggregates, since RET is highly dependent on the separation distance between the interacting chromophore units. As a consequence, and trying to reach a compromise between both factors, **QD1$_{OA}$**-**QD4$_{OA}$** were selected in this work in order to construct two different types of nanocrystal heteroaggregates with complementary properties: (a) **QD1$_{OA}$**-**QD2$_{OA}$** heteroaggregates, which should be easily recognized by TEM because of their large and different sizes, and by luminescence measurements because of their high PLQY; however, they

may suffer from inefficient RET due to the significant thickness of their ZnS shells; (b) **QD3$_{OA}$**-**QD4$_{OA}$** heteroaggregates, which should undergo much more efficient RET processes due to their narrow or none ZnS shells, but which will be more difficult to identify by TEM (due to the small dimensions of **QD4$_{OA}$**) and might present lower PLQY. In both cases, the HOMO-LUMO gaps of these pairs of QDs were designed to maximize the spectral overlap between them, which is a key parameter to promote RET processes, as already introduced in Chapter 4 and discussed in more detail in section V.2.3.3.

IV.2.2.2. Ligand exchange studies

Once synthesized and isolated, **QD1$_{OA}$**-**QD4$_{OA}$** were subjected to ligand exchange experiments to partially or totally replace oleic acid stabilizers with functional ligands **42**-**45**. As previously discussed, these compounds present two different types of functionalities for tethering to the surface of the nanocrystals: (a) carboxylic acid, and (b) thiol groups. Noticeably, these moieties do not only present distinct binding affinities towards CdSe and CdSe/ZnS QDs, but they can also critically influence their optical properties. Thus, many authors have demonstrated that thiolated stabilizers are not good capping ligands for pure core CdSe QDs, since they lead to the formation of new surface trap states that cause a substantial decrease of their PLQY.[54] This drawback is overcome when CdSe cores are protected with a ZnS shell, to which stabilizer sulfur atoms and sulfide groups strongly interact via dative bonds.[55] On the other hand, a good alternative to thiolated stabilizers for CdSe QDs are carboxylate ligands, which tightly bind to the Cd^{2+} ions on the QD surface without significantly altering its luminescence properties. In view of this, we first carried out preliminary ligand exchange experiments to determine which the best functionality was for the binding of the functional ligands to the QDs selected in this work.[48] In these experiments, **QD1$_{OA}$**, **QD4$_{OA}$**, **42** and **43** were taken as reference systems for CdSe/ZnS and CdSe nanocrystals, and carboxylated- and thiolated-azide ligands, respectively. For sake of simplicity, each one of the systems resulting from ligand exchange will be denoted by adding the number of the ligand introduced as a subindex label to the QD name (e.g. **QD1$_{42}$** for **QD1$_{OA}$** treated with carboxylic acid **42**).

In contrast to other stabilizers, ligand exchange processes in OA-coated QDs involving the introduction of new carboxylic acid or thiol stabilizers does not require any intermediate step and takes place directly by exposing the initial nanocrystals to a solution of the desired ligand.[9,56] This was therefore the methodology used in this work. To start with, **QD1$_{OA}$**-**42**, **QD1$_{OA}$**-**43**, **QD4$_{OA}$**-**42** and **QD4$_{OA}$**-**43** ligand exchanges were investigated by treating the nanocrystals of interest with different concentrations of azido-carboxylic acid **42** or azido-thiol **43** in chloroform solution, as shown in Figure IV-21A. ^{1}H NMR was then used to quantify the percentage of oleic acid ligand exchanged with **42** or **43** by deconvolution of the broad/narrow olefinic signals after ligand exchange. In agreement to the reported data for similar systems,[48] ligand exchange between the carboxylate groups of oleic acid and **42** took place almost immediately for both CdSe and CdSe/ZnS QDs, although it required proton transfer from the carboxylic acids introduced to the oleates released. By adding sufficient excess of new ligand **42**, nearly quantitative removal of the initial

stabilizer from the nanocrystal surface was achieved, as depicted in Figure IV-21B. However, poor stability of the resulting QD dispersions was observed when exceeding 40-50% exchange of the initial oleate stabilizers and the formation of a solid sediment was found after few hours (for **QD4₄₂**) or days (for **QD1₄₃**). Titration experiments perfomed for the **QD1$_{OA}$-42** system revealed that such instability arose from a non-equimolar replacement of oleic acid ligands by azido-carboxylic acid **42** at our experimental conditions. Thus, we determined that 7 OA molecules where exchanged with one **42** molecule when 100 % exchange was achieved. As such, this led to a lower stabilization of the resulting QDs and eventual aggregation and precipitation.
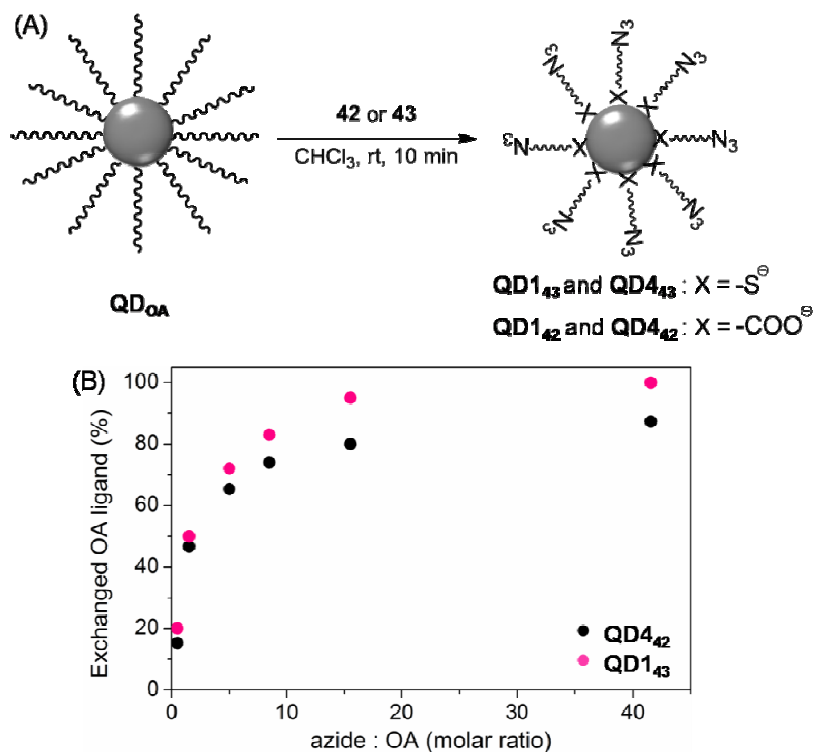
Figure IV-21. (A) Schematic representation of ligand exchange experiments conducted for the preparation of **QD₄₁** and **QD₄₂**. (B) Dependence of the OA exchange efficiency with the excess amount of new ligand **42** or **43** added, as determined by ^{1}H NMR.

QD1$_{OA}$-43 and **QD4$_{OA}$-43** exchanges were explored as an alternative way to introduce the functional ligands to the nanocrystals via thiolated groups (Figure IV-21A). As previously observed for **42**, fast exchange of oleate molecules by azido-thiol ligand **43** was observed in both cases, which also required proton transfer between the newly bound and released moieties. In addition, nearly quantitative exchange could also be achieved by using an excess of the thiolated stabilizer. In this case, however, high chemical stability was observed for the resulting QDs regardless of the extent of the ligand exchange process.

Regarding the influence of the introduced ligands on the QD optical properties, differences were also found between carboxylic acid and thiol ligands **42** and **43**, respectively, which were mainly related to the PLQY of the nanocrystals (Table IV-3). As already described,[54b] binding of thiolated stabilizer **43** to pure core CdSe **QD4** significantly quenched its photoluminescence, a detrimental

effect that was not observed when introducing carboxylic ligand **42**. Surprisingly, the opposite behavior was observed for core/shell **QD1**, its PLQY increasing upon thiol **43** binding. Such a result had only been reported for CdSe/ZnS nanocrystals when small amounts of thiol stabilizers were added, which were considered to reduce the number of electron traps on their surface.[57] A similar behavior was found in our case even when exchanging 100% of the initial oleic acid ligands, probably due to the very thick ZnS shell of the investigated QD (2.44 nm).[55]

Table IV-3. Photoluminescent quantum yields of **QD1** and **QD4** before and after oleic acid exchange by azido-carboxylic acid and azido-thiol ligands.

Ligand	QD1	QD4
OA	0.25	0.09
42[a]	0.18	0.13
43[a]	0.33	0.05

[a] PLQY determined for *ca.* 50% exchanged QDs. [b] PLQY determined for *ca.* 100% exchanged QDs.

Taking into account the results of our exploratory experiments, the following ligand exchange processes were performed to obtain the QDs coated with functional ligands to be used for SPAAC-induced aggregation:

1. OA-coated core/shell CdSe/ZnS QDs with thicker ZnS layers (i.e. **QD1$_{OA}$** and **QD2$_{OA}$**) were functionalized with azido-thiolated ligand **43** and cyclooctyne-thiolated ligand **45**, respectively, for which very large exchange efficiencies were expected (~100%) without detrimental effect on their PLQY. However, it must be noted that only around 50% of the new stabilizer molecules introduced in the case of **QD2$_{45}$** would correspond to active ligand **45**, since this compound could only isolated as a 1:1 mixture with non-reacting species **61**.
2. In spite of preventing complete ligand exchange, OA-coated core/shell CdSe/ZnS QDs with thin ZnS layers and OA-coated pure core CdSe QDs (i.e. **QD3$_{OA}$** and **QD4$_{OA}$**) were coated with carboxylated compounds **44** and **42**, which should allow preserving their PLQY.

Table IV-4 summarizes the main properties of the **QD1$_{43}$**, **QD2$_{45}$**, **QD3$_{44}$** and **QD4$_{42}$** resulting from these ligand exchange experiments. As observed in this table, both the exchange efficiencies and PLQY achieved are in agreement with the expected results predicted from our previous preliminary measurements.

Table IV-4. Final ligand exchange processes conducted and properties of the resulting QDs.

	QD1	QD2	QD3	QD4
Ligand introduced	43	45	44	42
OA ligand exchanged (%)	95	98	45	34
PLQY before ligand exchange	0.25	0.26	0.26	0.9
PLQY after ligand exchange	0.33	0.25	0.44	0.13

IV.2.3. Formation of QD-aggregates via SPAAC

The preparation of discrete, covalently-linked heteroaggregates of functionalized **QD1$_{43}$** and **QD2$_{45}$**, and **QD3$_{44}$** and **QD4$_{42}$** was carried out in CHCl$_3$ solution, room temperature and adjusting the concentration depending on the charaterization method used. The final outcome of the reactions assayed was monitored by means of ^{1}H NMR, TEM and photoluminescence measurements, with which we aimed to unambiguously demonstrate (i) the formation of the desired heteroaggregates, and (ii) the occurrence of resonance energy transfer processes between the different QDs in the assemblies.

IV.2.3.1. NMR analysis

Before performing ^{1}H NMR experiments on the QD aggregates obtained, we investigated the SPAAC reaction between free azide and cyclooctyne ligands. Since similar results were obtained for both **42**-**44** and **43**-**45** ligand pairs, here we will focus on the description of the SPAAC process between azido and cyclooctyne carboxylic acid derivatives **42** and **44**, which was conducted at room temperature in CHCl$_3$ (Scheme IV-20).
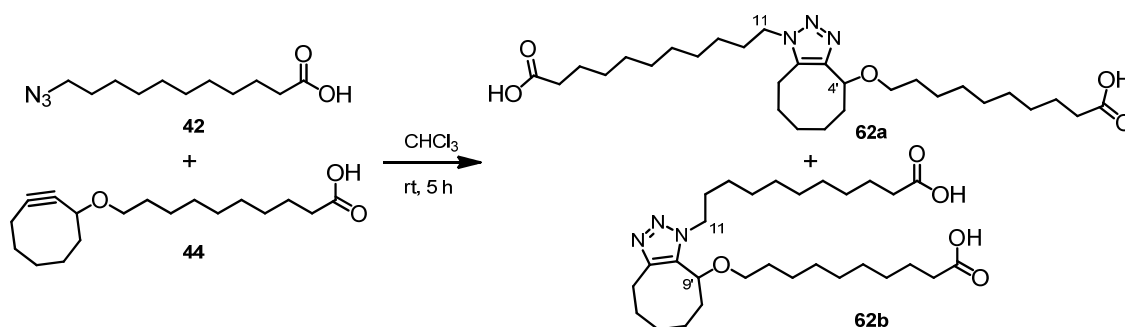
Scheme IV-20. Reaction conditions used to perform the SPAAC reaction between free ligands **42** and **44**, with led to a mixture of the 1,4- and 1,5-regioisomers of the 1,3-dipolar cycloaddition process, **62a** and **62b**, respectively.

Reaction controls by TLC showed complete conversion of the intial azide and cyclooctyne moieties in 3.5 h. Subsequent analysis of the reaction crude by ^{1}H NMR, ^{13}C NMR, COSY NMR and

Chapter IV
New functional ligands for quantum dot assembly
Results and discussion

HSQC NMR revealed both the formation of the 1,4- (**62a**) and 1,5-regioisomers (**62b**) of the 1,3-dipolar cycloaddition product in almost equal quantitites (1.2:1, Figure IV-22). Separate signals for each one of these isomers were especially distinguishable within the 4-5 ppm spectral region, where the resonances of H-4' (**62a**), H-9' (**62b**) and H-11 (**62a** and **62b**) were observed.
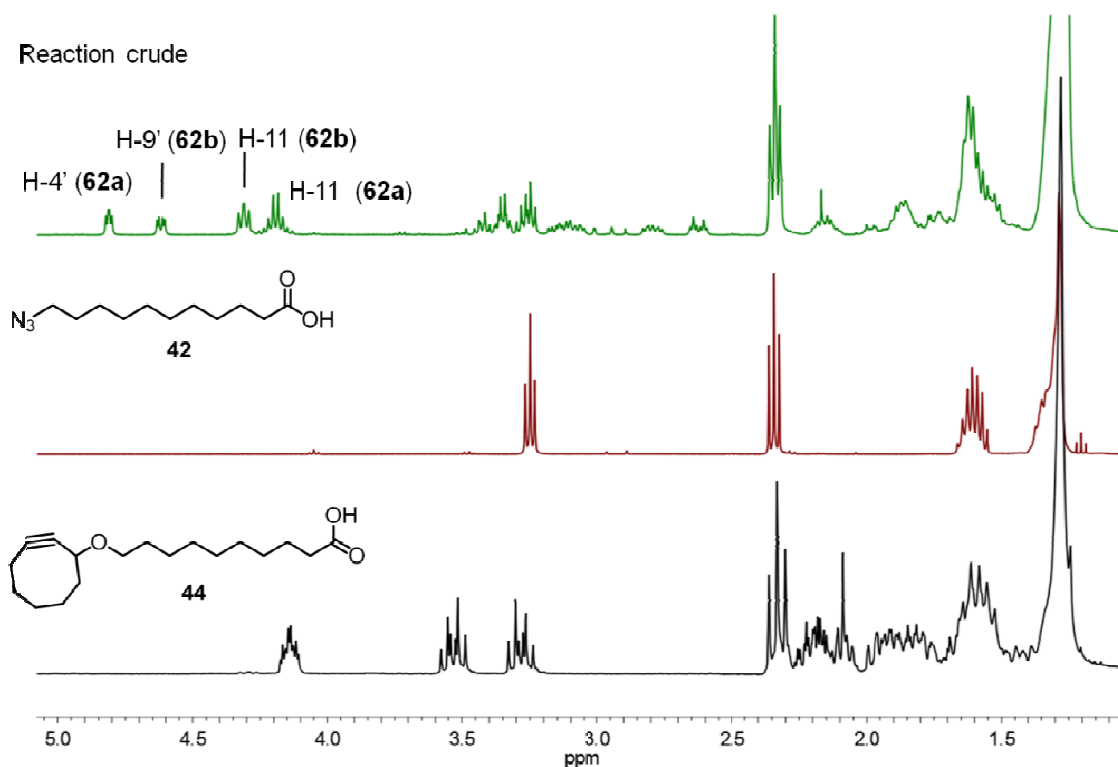
Figure IV-22. ^{1}H NMR (CDCl₃, 400 MHz) spectra of azide **42**, cyclooctyne **44** and the crude obtained by SPAAC reaction.

In order to correlate each set of signals in the ^{1}H NMR spectrum of the reaction crude with the corresponding regioisomer, NOESY NMR experiments were performed. NOESY is a 2D NMR experiment where cross peaks appear between signals arising from protons that are close-by in space.[47] Accordingly, the 1,4- and 1,5-regioisomers of the reaction may differ in the NOESY cross peaks between the aliphatic protons of their lateral alkyl chains, since they are pointing towards opposite sides of the molecule in the case of **62a** but lie almost parallel and closer in space in **62b**. As such, NOESY cross peaks between such protons were only expected for the latter. Indeed, this was the result observed in the NOESY NMR spectrum of the reaction crude, which is shown in Figure IV-23. Clearly, cross peaks were only detected between one of the two multiplets within the 4.5 - 5 ppm region and one of the signals corresponding to the H-11 nuclei in the *N*-bonded lateral chain. Such multiplets could then be unambiguously assigned to H-9' and H-11 in **62b**, which subsequently allowed disentangling the ^{1}H NMR signals corresponding to each regioisomer as well as determining their individual formation yields (45% and 55% for **62a** and **62b**, respectively).
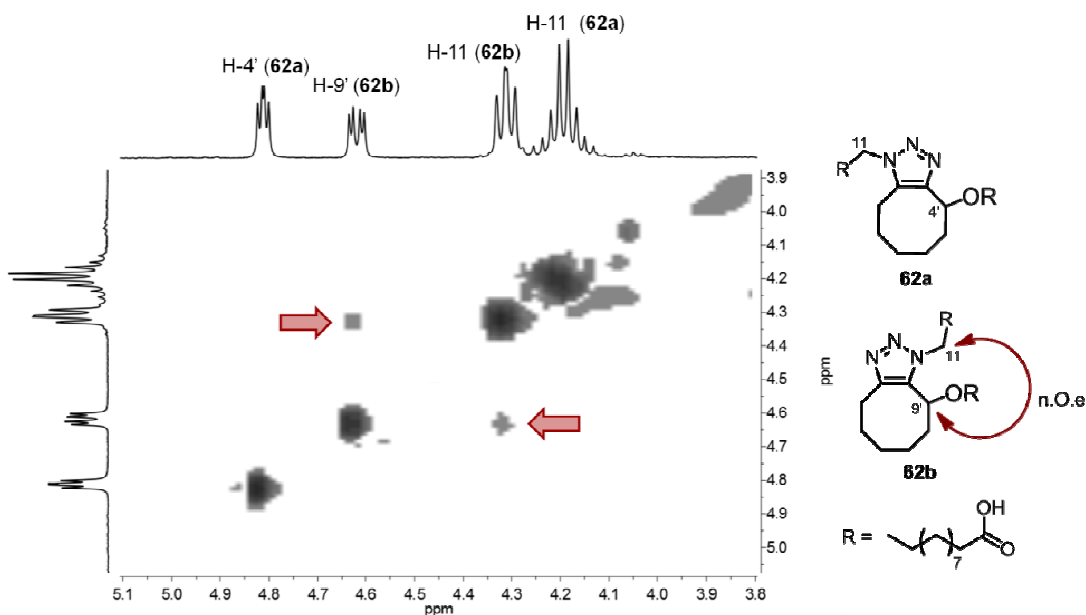
Figure IV-23. NOESY NMR (CDCl$_3$, 400 MHz) experiment of the SPAAC reaction crude.

Having investigated the SPAAC process between free ligands, we next moved to the study of the cycloaddition reaction between the azide and cyclooctyne ligands of **QD1$_{43}$**-**QD2$_{45}$** and **QD3$_{44}$**-**QD4$_{42}$**, with which we aimed to prepare materials **M13** and **M14**, respectively. Similar reaction conditions as those used for the free ligands were applied; namely, room temperature, CHCl$_3$ solution and 1:1 molar ratio with respect to the reacting ligands (Scheme IV-21). However, lower concentrations had to be used (~30-fold lower than in free ligand reaction), since we observed fast sedimentation of the QDs in concentrated CHCl$_3$ solutions. Consequently, reaction time was increased up to 24 h. After this time, unreacted QDs and QD-heteroaggregates were precipitated with MeOH, centrifuged and separated from mother liquors. The resulting solid materials were dried under vacuum and redispersed in CDCl$_3$ to perform NMR measurements.
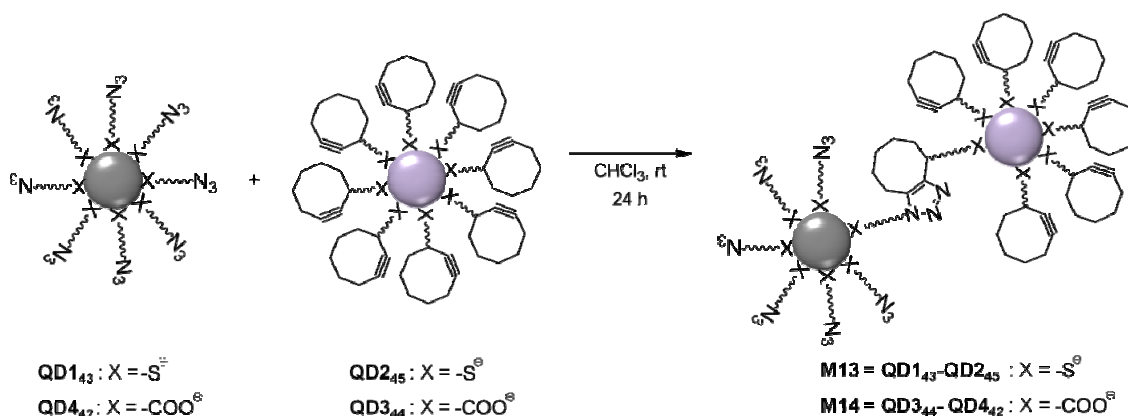
Scheme IV-21. Schematic representation and reaction conditions for the preparation of QD-heteroaggregates. For sake of simplicity, aggregates will be represented as dimers through all this section, although larger, more complex structures might be found due to the high percentage of surface functionalization with reacting ligands.

In particular, we focused on 1D DOSY NMR experiments, since they allowed selective detection of the organic ligands tethered to the surface of the nanocrystals. Thus, Figure IV-24 and Figure IV-25 plot the 4- to 5-ppm spectral region of the 1D DOSY NMR of **M14** and **M13**, respectively, where the most relevant signals to unambiguously prove the occurrence of the SPAAC reaction between QDs are expected (see Figure IV-22). For sake of clarity, there are also shown in these figures: (a) the ^{1}H NMR spectrum of the cycloadduct formed by reaction between the free ligands; (b) the ^{1}H NMR spectrum of the free cyclooctyne moiety involved in the process; and (c) the 1D DOSY NMR spectrum of such ligand after binding to QDs. The NMR data of the azide ligand is not given since it does not show any signal in the spectral range selected.

We first analyzed the spectral data for **M14** arising from the reaction between **QD3$_{44}$** and **QD4$_{42}$**, since (i) the process was conducted with a larger amount of starting materials, and (ii) ligands **44** and **42** had been obtained pure. Therefore, only the signals corresponding to cyclooctyne **44** and the product of the cycloaddition reaction should be found in the spectral area investigated, as indeed observed in Figure IV-24. Noticeably, the signal at 4.15 ppm arising from the unreacted cyclooctyne group in **QD3$_{44}$** largely decreased in intensity in the spectrum of **M14**, which instead presents new signals at 4.31, 4.63 and 4.83 ppm that can be assigned to the cycloaddition products. In fact, comparison with the ^{1}H NMR spectrum of the free cycloadduct indicates that mainly the 1,5-regiosiomer of this compound is formed in the reaction between QDs. Surprisingly, the formation of this isomer seems to be favored when SPAAC takes place between ligands sitting onto the surface of adjacent nanocrystlas, probably due to the tight orientational requirements of this cycloaddition reaction.[58]
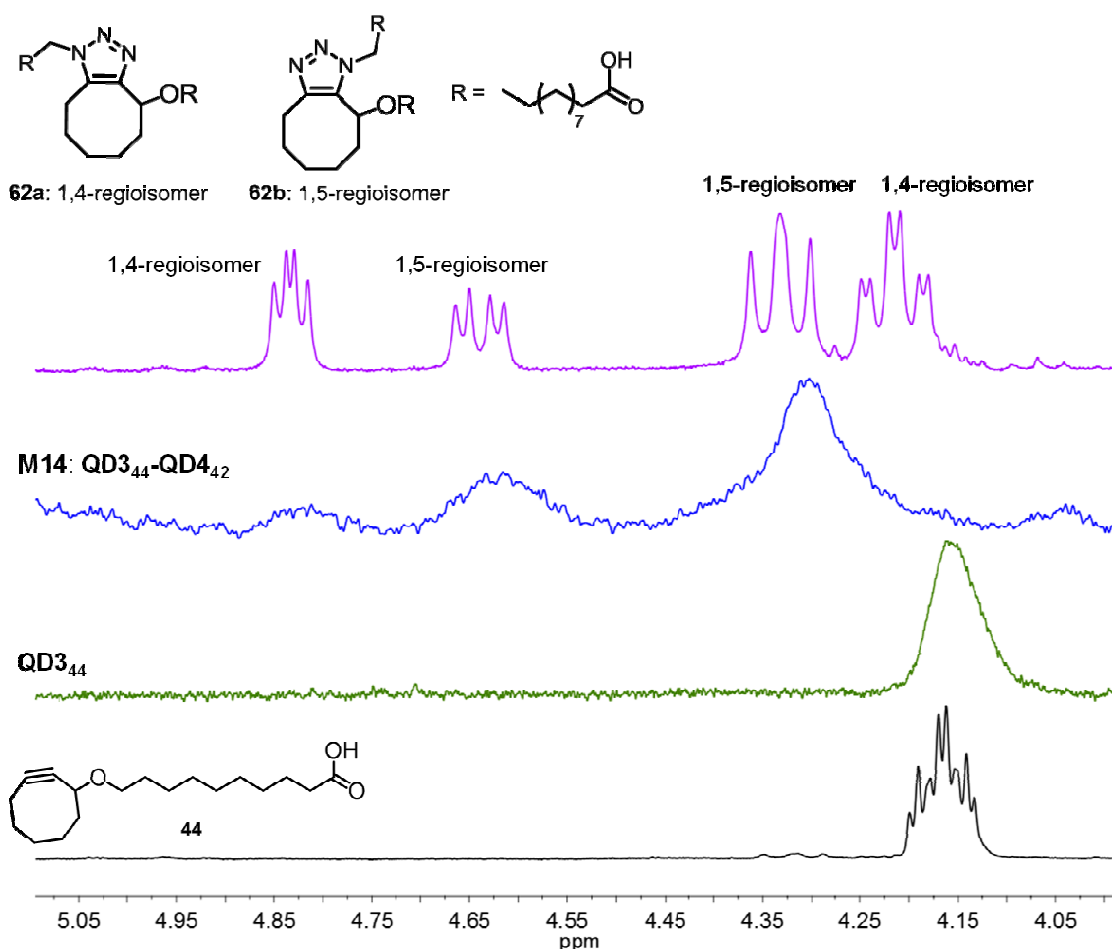
Figure IV-24. 4– to 5-ppm region of the ^{1}H NMR (CDCl$_3$, 400 MHz) of the SPAAC product for the reaction between free ligands, 1D DOSY NMR of **M14**, 1D DOSY NMR of **QD3$_{44}$** bearing the cyclooctyne reacting group and ^{1}H NMR of free ligand **44**.

Similar results were found for **M13** formed by reaction between **QD1$_{43}$** and **QD2$_{45}$** (Figure IV-25). In this case, however, the analysis of its 1D DOSY NMR became more complex because of: (a) its significantly worse signal-to-noise ratio, which we mainly ascribe to the smaller amount of starting materials used for the cycloaddition reaction, and (b) the presence of a signal at 4.30 ppm arising from the unreacting ligand **61** that could not be separated from target cyclooctyne **45** during the synthesis of this compound and the ligand exchange process. Unfortunately, this signal fully overlaps with the expected at 4.31 ppm for the 1,5-regioisomer of the cycloaddition reaction. Nevertheless, the intensity decrease observed for the cyclooctyne signal at 4.15 ppm and the occurrence of a new broad, shallow signal at 4.65 ppm suggests that SPACC took place between **QD1$_{43}$** and **QD2$_{45}$**. Together with the results obtained for **M14**, this clearly demonstrates the viability of exploiting this cycloaddition reaction to undertake controlled QD heteroaggregation.
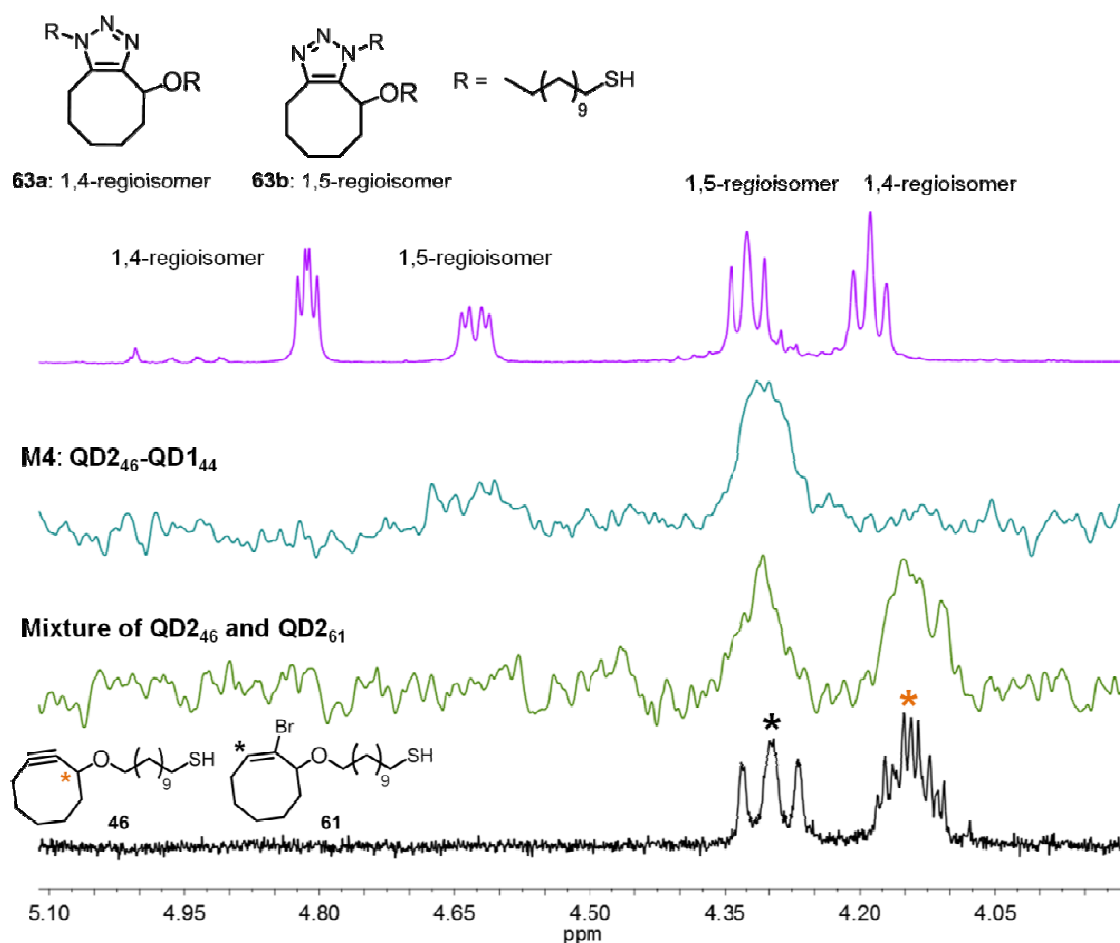
Figure IV-25. 4- to 5-ppm region ^{1}H NMR (CDCl$_3$, 400 MHz) of the SPAAC product for the reaction between free ligands, 1D DOSY NMR of **M14**, 1D DOSY NMR of the mixture **QD2$_{45}$** and **QD2$_{61}$** and ^{1}H NMR of the mixture of free ligand **45** and impurity **61**.

IV.2.3.2. Electron microscopy analysis

Once confirmed the formation of QD cycloadducts by means of 1D diffusion NMR, new experiments were conducted to morphologically characterize the resulting aggregates by means of TEM. Since electron microscopy measurements were carried out in combination with photoluminescence experiments (see section V.2.3.3), the reaction conditions shown in Scheme IV-21 for promoting the assembly of QDs were slightly varied. In particular, the concentrations of the starting individual QDs were tuned to ensure similar values of emission intensities at t=0 for the two types of nanocrystals mixed (1:1.1 and 1:4 for **QD1$_{43}$-QD2$_{45}$** and **QD3$_{44}$-QD4$_{42}$**). In this way, changes in photoluminescence observed upon QD heteroaggregation could be better detected and analyzed.

For electron microscopy analysis, aliquots of the reaction mixtures were taken both at the initial (t = 0 h) and final (t = 24 h) stages of the process. To prevent unspecific QD aggregation, these samples were then deposited onto carbon grids by spin-coating instead of drop-casting, and they were finally analyzed by TEM.

Noticeably, individual, well-separated QDs of different sizes were mainly observed at t=0 for both reaction mixtures, which demonstrated that efficient nanocrystal dispersion had been achieved by spin-coating. As such, QD heteroaggregates detected at t=24 h could be ascribed to SPAAC-induced assemblies. Indeed, the formation of such aggregates was observed in the TEM images of both **M13** and **M14**, as clearly shown in the zoom-ins given in Figure IV-26 and Figure IV-27. Detailed analysis of these images allowed us concluding:

1. QDs of different sizes were arranged in close contact in the heteroaggregates of both **M13** and **M14** (see green circles in Figure IV-26B and Figure IV-27B). In addition, their average center-to-center distances ((10.2 ± 2.6) nm and (7.19 ± 1.31) nm, respectively) were in agreement with the values expected taking into account the sizes of the nanocrystals involved and the end-to-end lengths of the 1,5-regioisomer of the cycloadducts formed by SPAAC[d] (9.77 and 6.18 nm, respectively). These are therefore clear proofs that we achieved for the first time SPAAC-induced, covalent heteroaggregation of QDs.

2. QD heteroaggregates containing different number and ratio of their constituent nanocrystals were obtained for both **M13** and **M14**. We ascribed this result to the large population of functional ligands onto the QD surface, which did not enable accurate control of the extent and stoichiometry of the aggregation process. Nevertheless, it must be noted that only discrete QD heteroaggregates were observed in our TEM images and no evidence of the formation of massive nanocrystal assemblies was found. As next discussed, this might indicate low reaction probabilities between the azido and cyclooctyne groups located onto the surface of different QDs.

3. After 24 h, only partial aggregation of the QDs was achieved and the presence of individual, non-reacted nanocrystals was also observed for both **M13** and **M14** by TEM (see red circles in Figure IV-26B and Figure IV-27B). This is in contrast to the NMR data shown in the previous section, where nearly complete disappearance of the signals corresponding to QD-bound, unreacted cyclooctyne moieties was observed. Provided that impurity **60** did remain tethered to the nanocrystal surface in **M13** after SPAAC, QD-unbinding of the reactive ligands during the cycloaddition process can hardly account for the NMR result, the reason for which is still not clear to us.[e] Actually, from the statistical analysis of several electron microscopy images, we determined that the 73 % of **QD1$_{43}$** and the 77 % of **QD3$_{44}$** had reacted to form nanocrystal heteroaggregates in **M13** and **M14**, respectively. This result indicates that the reaction between these two ligands took place with high probabilities and the steric congestion around the reactive functional groups in the close-packed monolayers of molecules coating the nanocrystals and/or

---

[d] The end-to-end distances of the 1,5-regioisomer of the cycloaddition between ligands **43**-**45** and **42**-**44** were determined upon geometrical optimization at the MM2 calculation level with ChemBioOffice 2010.

[e] Other factors such as the difference in concentration and reactant ratio between the samples analyzed by ^{1}H NMR and TEM could explain the discrepancies observed for the results obtained with these techniques.

the limited relative mobilities of QD-bound ligands with respect to those in free solution do not influence the tight conformational and orientational requirements of SPAAC.[58]
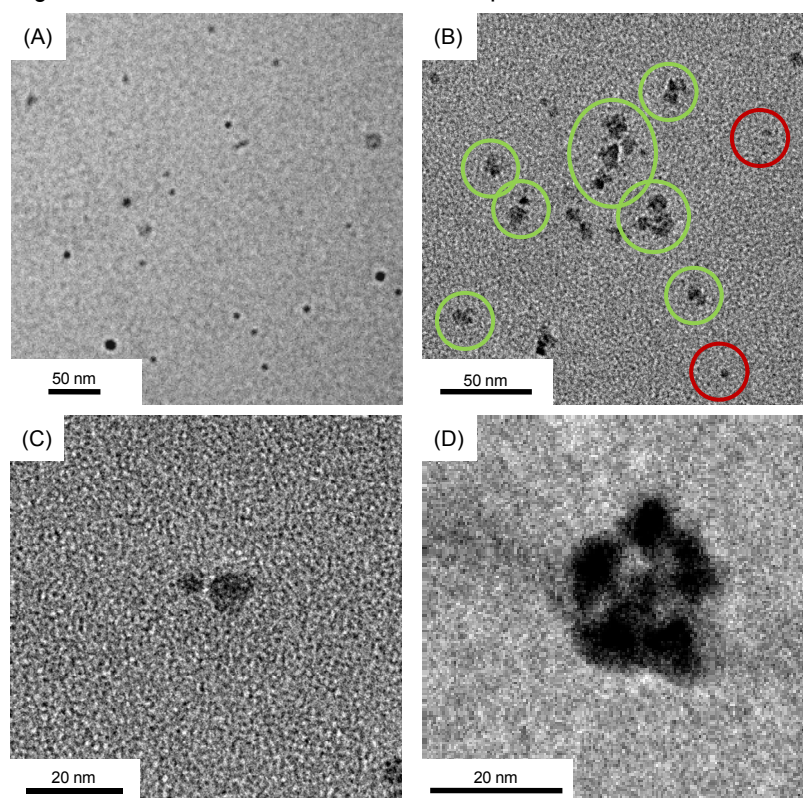
Figure IV-26. TEM images of **M13** at (A) t = 0 h and (B-D) t = 24 h. Red and green circles in (B) indicate isolated and aggregated QDs, respectively.
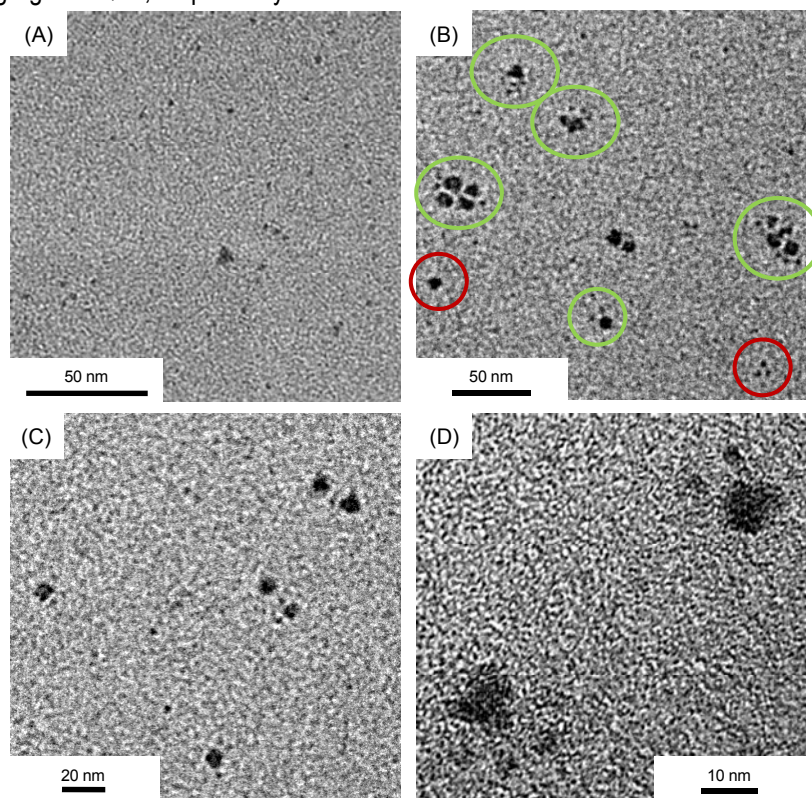

Figure IV-27. TEM images of **M14** at (A) t = 0 h and (B-D) t = 24 h. Red and green circles in (B) indicate isolated and aggregated QDs, respectively.

109

IV.2.3.3. Optical properties analysis

The same QD reaction mixtures monitored by TEM (see section V.2.3.2) were simultaneously investigated by means of steady-state and time-resolved optical measurements. While negligible changes were observed in the absorption spectra of such mixtures with reaction time, significant variation of their photoluminescence spectra was found to occur. This is clearly illustrated by Figure IV-28, which depicts the emission spectra of the reaction mixtures leading to **M13** and **M14** at t=0, 5 and 24 h.
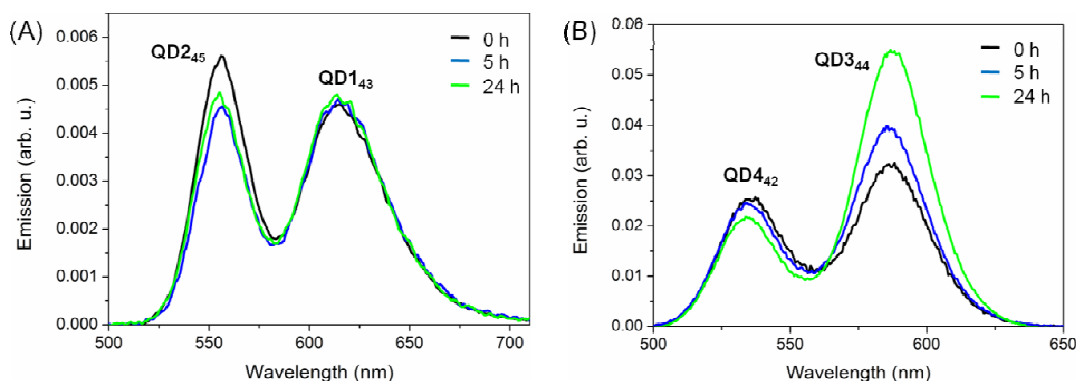
Figure IV-28. Time dependence of the PL spectra of the reaction mixtures leading to the formation of (A) **M13** and (B) **M14**: t= 0, 5 and 24 h, and λ_{exc} = 473 nm. In all cases, the emission bands corresponding to each of the QDs mixed were sufficiently separated as their maxima to be univocally identified at (i) 623 and 550 nm for **QD1₄₃** and **QD2₄₅** in **M13**, and (ii) 593 and 532 nm for **QD3₄₄** and **QD4₄₂** in **M14**.

Noticeably, the luminescence intensity of the QDs with the highest bandgap in each material (**QD2₄₅** in **M13** with $\lambda_{max,Em}$ = 550 nm and **QD4₄₂** in **M14** with $\lambda_{max,Em}$ = 532 nm) decreased with reaction time, whereas that corresponding to the lowest bandgap QDs concomitantly increased (**QD1₄₃** in **M13** with $\lambda_{max,Em}$ = 623 nm and **QD3₄₄** in **M14** with $\lambda_{max,Em}$ = 593 nm). The occurrence of resonance energy transfer processes between adjacent QDs in the heteroaggregates formed is the most plausible explanation for this result owing to the large spectral overlap between the emission spectra of **QD2₄₅** and **QD4₄₂**, and the absorption spectra of **QD1₄₃** and **QD3₄₄**, respectively (Figure IV-29).
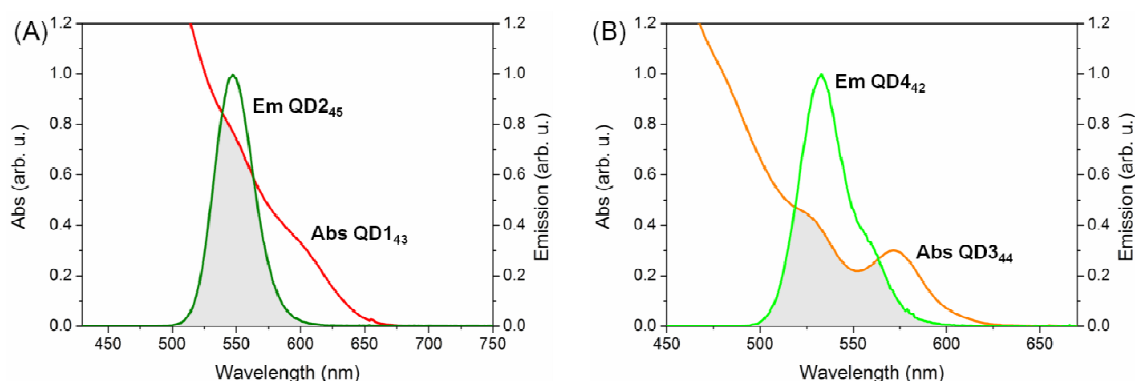
Figure IV-29. Spectral overlaps for **QD1₄₃**-**QD2₄₅** and **QD3₄₄**-**QD4₄₂**.

As discussed in chapter IV, RET is a non-radiative dipole-dipole mechanism through which electronic excitation energy can take place on the nanoscale from high excitation energy donors (in our case, **QD2**$_{45}$ in **M13** and **QD4**$_{42}$ in **M14**) towards lower excitation energy acceptors (**QD1**$_{43}$ in **M13** and **QD3**$_{44}$ in **M14**). When both species are luminescent, this should therefore result in quenching of the donor emission and enhancement of the acceptor emission, as observed in Figure IV-28. Based on these spectral changes, RET efficiency can be easily calculated using Equation (IV-2), where I_D and I_{DA} are the emission intensities of the donor in the absence or presence of the acceptor (in our case, at t=0 and 24 h, respectively):

$$E = 1 - \frac{I_{DA}}{I_D}$$

(IV-2)

By spectrally decomposing the photoluminescence measurements in Figure IV-28 and selectively integrating the emission intensity arisen from **QD2**$_{45}$ and **QD4**$_{42}$, the following RET efficiencies were calculated: 22 and 17 % for **M13** and **M14**, respectively. It must be noted that these values significantly underestimate the actual resonance energy transfer efficiencies in the heteroaggregates prepared, since a large amount of individual, non-reacted QDs were still observed in the reaction mixtures at t=24 h. Since negligible energy transfer processes were expected for those QDs owing to the high dilution conditions at which photoluminescence measurements were conducted, a more accurate estimation of the RET efficiencies in **M13** and **M14** was obtained by taking into account the reaction efficiencies determined by means of TEM and applying Equation IV-3, where X_b corresponds to the molar fraction of bonded **QD2**$_{45}$ or **QD4**$_{42}$:

$$E = \frac{1}{X_b} - \frac{I_{DA}}{X_b \cdot I_D}$$

(IV-3)

In this way, resonance energy transfer efficiencies were finally determined to be 29 % and 85 % for **M13** and **M14**, respectively. To investigate the large difference in experimental RET efficiencies found for **M13** and **M14**, a theoretical estimation was made according to equations III-1 and III-2 in Chapter III, which allowed calculation, first, of the Förster radius of each acceptor-donor pair and, finally, of the expected energy transfer efficiencies. To apply these equations, molar absorption coefficients of the donor QDs had to be first estimated using expression IV-4, where D is the core diameter of the nanocrystal of interest (see Table IV-2):[48]

$$\varepsilon = 5857 \cdot D^{2.65}$$

(IV-4)

Next, the spectral overlap between donor emission and acceptor absorption was determined from Figure IV-29 and used together with donor PLQY to calculate the following R_0 values: 4.09 and 3.94 nm for **M13** and **M14**, respectively, assuming random orientation of the transition dipoles ($\kappa^2 =$

2/3) (Table IV-5). Clearly, both materials exhibited very similar Förster radii, which meant that differences in RET efficiency could be directly ascribed to distinct QD separation distances in the heteroaggregates.

Table IV-5. Data for the theoretical determination of R_0 and E for **M13** and **M14**.

	$\varepsilon_{Acceptror}$	Φ_{Donor}	J	R_0 (nm)	r_{QD} (nm)	E (%)
M13	95879.78	0.25	$2.10 \cdot 10^{-13}$	4.09	6.00	9
M14	72715.23	0.13	$3.23 \cdot 10^{-13}$	3.94	3.14	80

In view of this, estimates of the CdSe core-to-core distance (r_{QD}) between adjacent QDs in **M13** and **M14** were performed using the shell dimensions of the nanocrystals (see Table IV-2) and the average QD separation measured from TEM images (see section V.2.3.2). In this way, r_{QD}= 6.00 and 3.14 nm were determined for the donor-acceptor pairs in **M13** and **M14**, which finally allowed calculation of the predicted RET efficiencies for both materials: E= 9 and 80 % (Table IV-5). Although these values somewhat underestimated the experimental RET efficiencies determined for **M13**, they clearly proved that: (a) resonance energy transfer processes should occur between different QDs in the heteroaggregates of **M13** and **M14**, and (b) larger RET efficiencies should be exhibited by **M14** based on adjacent QD separation, as experimentally observed.

A further proof of the occurrence of energy transfer processes in **M13** and **M14** was obtained by means of photoluminescence lifetime experiments. Figure IV-30 shows the emission time decays at t=0 and 24 h of the high band gap QDs in the reaction mixtures prepared for the synthesis of **M13** and **M14** (i.e. the energy donors **QD2$_{45}$** and **QD4$_{42}$**). In all cases, non-monoexponential decay curves were measured, a feature that has been previously reported for both pure core CdSe[59] and gradient core/shell CdSe/ZnS[60] QDs and has been ascribed to the recombinations of delocalized exciton in the internal core states and localized exciton in the surface states.[61] In our case, tentative biexponential fits of these time profiles were attempted, which reasonably reproduced the experimental data and revealed the occurrence of fast and slow decay components (Table IV-6). The kinetic data retrieved for such fast component should however be only taken as rough estimates of the actual values, because in all cases it presented shorter lifetimes ($\tau_1 > 2.5$ ns) than the instrumental response function of our measurements (laser pulse width $\sim$ 6 ns).
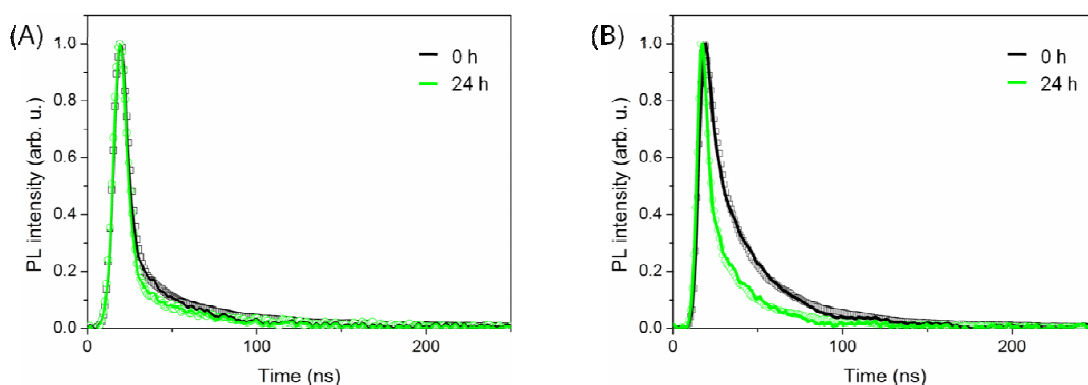
Figure IV-30. Normalized excited states lifetime decays of the initial (t=0) and final (t=24 h)reaction mixtures prepared for the synthesis of (A) **M13** and (B) **M14** (λ_{exc} = 355 nm 355 nm, λ_{det} = 540 nm). Solid lines correspond to biexponential fits of the experimental data.

Table IV-6. Amplitudes and lifetimes determined from biexponential fits of the photoluminescence decays measured during theformation of **M13** and **M14**.

		A_1	τ_1 (ns)	A_2	τ_2 (ns)
M13	0 h	0.91	1.05	0.09	16.4
	24 h	0.97	0.78	0.03	32.6
M14	0 h	0.7	2.26	0.3	25.6
	24 h	0.96	0.41	0.04	20.4

In spite of this, clear changes in the overall decay curves and its two components could be observed upon formation of **M13** and **M14**, that is to say, upon QD heteroaggregation. In both cases, the radiative luminescence kinetics of the high bandgap nanocrystals in the mixtures was found to increase after 24 h, which was mainly due to larger rate and/or contribution of the fast component (see Table IV-6). This effect is a definitive proof that quenching of the luminescence of **QD2$_{45}$** and **QD4$_{42}$** occurred upon SPAAC-induced tethering to lower bandgap nanocrystals **QD1$_{43}$** and **QD3$_{44}$**, a situation that has been previously reported for QD heteroaggregates.[22] Although different interparticle processes such as resonance energy transfer or photoinduced electron transfer could account for this behavior, we considered the former mechanism to play the most important contribution in our case since concomitant increments in QD acceptor emission were measured (see Figure IV-28). In addition, good agreement was found between our steady-state and time-resolved measurements, because larger changes upon aggregation were determined both in emission spectra and decays for **M14**. As previously discussed, this was the material where shorter distances were achieved between the donor and acceptor CdSe cores, thus maximizing RET efficiency.

IV.3. CONCLUSIONS

In this chapter, strain-promoted azido alkyne cycloaddition was explored as a new methodology to prepare for the first time discrete, covalently-linked heteroaggregates of QDs. For this purpose, the following experiments were conducted:

1. Four different functional ligands were synthesized to promote SPAAC-induced QD assembly: compounds **42** (1 step, 99 % yield), **43** (4 steps, 60 % yield), **44** (3 steps, 37 % yield) and **45** (50% purity in 5 steps and with a 4 % yield). These ligands present both different terminal moieties for QD-tethering (**42**, **44**: carboxylic acid; **43**, **45**: thiol) and mutually reactive groups enabling Cu-free 1,3-dipolar cycloaddition at room temperature (**42**, **43**: azide; **44**, **45**: cyclooctyne).

2. Four different oleic acid-coated QDs were prepared: 3 core/shell CdSe/ZnS (**QD1$_{OA}$**-**QD3$_{OA}$**) and 1 pure core CdSe (**QD4$_{OA}$**) nanocrystals. Their optical properties and sizes were chosen to favor identification of the QD heteroaggregates formed via SPAAC and enable excited state energy transfer processes in the resulting assemblies.

3. Oleic acid ligands in the QDs were exchanged by the functionalized ligands. After optimization of exchange conditions, an average of 40 % and 96 % of carboxylated ligands and thiolated ligands were introduced in the nanocrystal surface, respectively. This led to stable colloidal QDs functionalized with azide (**QD1$_{43}$**, **QD4$_{42}$**) and cyclooctyne (**QD2$_{45}$** and **QD3$_{44}$**) reactive groups.

4. Pairs of the functionalized QDs, **QD1$_{43}$**-**QD2$_{45}$** and **QD3$_{44}$**-**QD4$_{42}$**, were mixed to promote SPAAC reaction to form QD-heteroaggregates **M13** and **M14**, respectively. Both materials were analyzed by NMR, TEM and photoluminescence techniques that clearly showed selective reactivity between azide and cyclooctyne groups leading to nanocrystal assembly. According to total reactivity observed by NMR, high reaction efficiencies were determined by TEM (73 % for **M13** and 77 % for **M14**). Moreover, energy transfer processes were observed for both materials with efficiencies of 29 % and 85 %, respectively. Separation between the core of the nanocrystals plays an important role in these processes, which can be modulated by rationally tuning the size of the capping shell.

In conclusion, we demonstrated in this chapter the SPAAC-induced formation of QD heteroaggregates that displayed RET efficiencies as high as 82 % between different, adjacent nanocrystals by properly tuning the separation between their emissive cores. This opens up the door for future application of this methodology to the construction of 1D assemblies of well-ordered QDs that could behave as photonic wires for the efficient and unidirectional transport of excitation energy on the nanoscale.

IV.4. REFERENCES

1 J. Y. Kim, O. Voznyy, D. Zhitomirsky, E. H. Sargent, *Adv. Mater.* **2013**, *25*, 4986-5010.

2 I. L. Medintz, H. T. Uyeda, E. R. Goldman, H. Mattoussi, *Nat. Mater.* **2005**, *4*, 435-446.

3 C. de M. Donegá, *Chem. Soc. Rev.* **2011**, *40*, 1512-1546.

4 R. Rossetti, S. Nakahara, L. E. Brus, *J. Chem. Phys.* **1983**, *79*, 1086-1088.

5 C. B. Murray, D. J. Norris, M. G. Bawendi, *J. Am. Chem. Soc.* **1993**, *115*, 8706-8715.

6 H. Liu, J. S. Owen, A. P. Alivisatos, *J. Am. Chem. Soc.* **2007**, *129*, 305-312.

7 (a) V. Klimov, P. H. Bolivar, H. Kurz, *Phys. Rev. B* **1996**, *53*, 1463-1467. (b) V. I. Klimov, D. W. McBranch, *Phys. Rev. Lett.* **1998**, *80*, 4028-4031.

8 (a) B. O. Dabbousi,; J. Rodriguez-Viejo, F. V. Mikulec, J. R. Heine, M. G. Bawendi, *J. Phys. Chem. B* **1997**, *101*, 9463–9475. (b) M. A. Hines, P. Guyot-Sionnest, *J. Phys. Chem.* **1996**, *100*, 468–471.

9 W. K. Bae, K. Char, H. Hur, S. Lee, *Chem. Mater.* **2008**, *20*, 531-539.

10 J. Cho, Y. K. Jung, J-K. Lee, *J. Mater. Chem.* **2012**, *22*, 10827-10833.

11 X. Michalet, F. F. Pinaud, L. A. Bentolila, J. M. Tsay, S. Doose, J. J. Li, G. Sundaresan, A. M. Wu, S. S. Gambhir, S. Weiss, *Science* **2005**, *307*, 538-544.

12 D. L. Klein, R. Roth, A. K. L. Lim, A. P. Alivisatos, P. L. McEuen, *Nature* **1997**, *389*, 699-701.

13 W. C. W. Han, S. Nie, *Science* **1998**, *281*, 2016-2018.

14 (a) B. A. Kairdolf, A. M. Smith, T. H. Stokes, M. D. Wang, A. N. Young, S. Nie, *Annu. Rev. Anal. Chem.* **2013**, *6*, 143-162. (b) D. V. Talapin, C. B. Murray, *Science* **2005**, *310*, 86-89.

15 H. Shen, Q. Lin, H. Wang, L. Qian, Y. Yang, A. Titov, J. Hyvonen, Y. Zheng, L. S. Li, *ACS Appl. Mater. Interfaces* **2013**, *5*, 12011-12016.

16 (a) P. K. Santra, P. V. Kamat, *J. Am. Chem. Soc.* **2013**, *135*, 877-885. (b) A. Kongkanand, K. Tvrdy, K. Takechi, M. Kuno, P. V. Kamat, *J. Am. Chem. Soc.* **2008**, *130*, 4007-4015.

17 I. Gur, N.. A. Fromer, M. L. Geier, A. P. Alivisatos, *Science* **2005**, *310*, 462-465.

18 F. Xu, C. R. Haughn, X. Ma, M. F. Doty, S. G. Cloutier, *Appl. Phys. Lett.* **2014**, *104*, 51112-51115.

19 M. Nikumbh, V. Gore, R B. Gore, *Ren. Energ.* **1997**, *11*, 459-467.

20 (a) X. Peng, T. E. Wilson, A. P. Alivisatos, P. G. Schultz, *Angew. Chem. Int. Ed.* **1997**, *36*, 145-147. (b) R. Koole, P. Liljeroth, C. de M. Donegá, D. Vanmaekelbergh, A. Meijerink, *J. Am. Chem. Soc.* **2006**, *128*, 10436-10441. (c) X. Xu, S. Stöttinger, G. Battagliarin, G. Hinze, E. Mugnaioli, C. Li, K. Müllen, T. Basché, *J. Am. Chem. Soc.* **2011**, *133*, 18062-18065.

[21] (a) D. Gross, A. S. Susha, T. A. Klar, E. Da Como, A. L. Rogach, J. Feldmann, *Nano Lett.* **2008**, *8*, 1482-1485. (b) M. Wu, P. Mukherjee, D. N. Lamont, D. H. Waldeck, *J. Phys. Chem. C* **2010**, *114*, 5751-5759.

[22] G. Tikhomirov, S. Hoogland, P. E. Lee, A. Fischer, E. H. Sargent, S. O. Kelley, *Nat. Nanotech.* **2011**, *6*, 485-490.

[23] C.Zhang, R. J. ;acfarlane, K. L. Young, C. H. J. Choi, L. Hao, E. Auyeung, G. Liu, X. Zhou, C. A. Mirkin, *Nat. Mater.* **2013**, *12*, 741-746.

[24] F. A. Carey, R. J. Sundberg, *Advanced Organic Chemistry*, *Part C: Reactions and Synthesis* (4th Ed.). Springer science + Business media: New York, **2000**.

[25] F. Himo, T. Lovell, R. Hilgraf, V. V. Rostovtsev, L. Noodleman, K. B. Sharpless, V. V. Fokin, *J. Am. Chem. Soc.* **2005**, *127*, 210-216.

[26] D. Janczewski, N. Tomczak, S. Liu, M-Y. Han, G. J. Vancso, *Chem. Commun.* **2010**, *46*, 3253-3255.

[27] N. J. Agard, J. A. Prescher, C. R. Bertozzi, *J. Am. Chem. Soc.* **2004**, *126*, 15046-15047.

[28] J. C. Jewett, C. R. Bertozzi, *Chem. Soc. Rev.* **2010**, *39*, 1272-1279.

[29] A. Bernardin, A. Cazet, L. Guyon, P. Delannoy, F. Vinet, D. Bonnaffé, I. Teixer, *Bioconj. Chem.* **2010**, *21*, 583-588.

[30] J. Hernando, P. A. J. de Witte, E. M. H. P van Dijk, J. Korteik, R. J. M. Nolte, A. E. Rowan, M. F. García-Parajó, N. F. van Hulst, *Angew. Chem. Int. Ed.* **2004**, *43*, 4045-4049.

[31] J. Y. Yao, C. Uttamapinant, A. Poloukhtine, J. M. Baskin, J. A. Codelli, E. M. Sletten, C. R. Bertozzi, V. V. Popik, A. Y. Ting, *J. Am. Chem. Soc.* **2012**, *134*, 3720-3728.

[32] A. B. Neef, C. Schultz, *Angew. Chem. Int. Ed.* **2009**, *48*, 1498-1500.

[33] J. P. Collman, N. K. Devaraj, C. E. D. Chidsey, *Langmuir* **2004**, *20*, 1051-1053.

[34] (a) M. E. Pérez-Ojeda, B. Trastoy, I. López-Arbeloa, J. Bañuelos, A. Costela, I. García-Moreno, J. L. Chiara, *Chem. Eur. J.* **2011**, *17*, 13258-13268. (b) D. M. Nguyen, D. H. Miles, *Synthetic Commun.* **2011**, *41*, 1759-1771.

[35] M. Wijtmans, S. J. Rosenthal, B. Zwanenburg, N. A. Porter, *J. Am. Chem. Soc.* **2006**, *128*, 11720-11726.

[36] S. Warren, P. Wyatt, *Organic Synthesis, The Disconnection Approach* (2nd Ed). Chichester John Wiley & Sons: United Kingdom, **2008**, pp. 66-75.

[37] J. Clayden, N. Greeves, S. Warren, P. Wothers, *Organic Chemistry* (2nd. Ed). Oxford: New York, **2001**.

[38] Y-Y. Lin, S-C. Tsai, S. J. Yu, *J. Org. Chem.* **2008**, *73*, 4920-4928.

[39] W. von E. Doering, A. K. Hoffmann, *J. Am. Chem. Soc.* **1953**, *76*, 6162-6165.

40 M. Fedorynski, *Chem. Rev.* **2003**, *103*, 1099-1132.

41 C. B. Reese, A. Shaw, *J. Am. Chem. Soc.* **1970**, *92*, 2566-2568.

42 S. I. Kozhushkov, M. Bandl, A. de Meijere, *Eur. J. Org. Chem.* **1998**, 1535-1542.

43 K. C. Nicolaou, G. Zuccarello, C. Riemer, V. A. Estevez, W-M. Dai, *J. Am. Chem. Soc.* **1992**, *19*, 7360-7371.

44 B. D. Fairbanks, E. A. Sims, K. S. Anseth, C. N. Bowman, *Macromolecules* **2010**, *43*, 4113-4119.

45 W. W. Yu, X. Peng, *Angew. Chem. Int. Ed.* **2002**, *41*, 2368-2371.

46 (a) I. Moreels, B. Fritzinger, J. C. Martins, Z. Hens, *J. Am. Chem. Soc.* **2008**, *130*, 15081-15086. (b) X. Ji, D. Copenhaver, C. Sichmeller, X. Peng, *J. Am. Chem. Soc.* **2008**, *130*, 5726-5735.

47 T. D. W. Claridge, High-Resolution NMR techniques in organic chemistry. Elsevier: Oxford. **2009**.

48 B. Fritzinger, R. K. Capek, K. Lambert, J. C. Martins, Z. Hens, *J. Am. Chem. Soc.* **2010**, *132*, 10195-10201.

49 J. S. Owen, J. Park, P-E. Trudeau, A. P. Alivisatos, *J. Am. Chem. Soc.* **2008**, *130*, 12279-12281.

50 (a) E. Gomes, A. Hassinen, A. Szczygiel, Q. Zhao, A. Vantomme, J. C. Martins, Z. Hens, *Phys. Chem. Lett.* **2011**, *2*, 145-152. (b) A. J. Morris-Cohen, M. Malicki, M. D. peterson, J. W. J. Slavin, E. A. Weiss, *Chem. Mater.* **2013**, *25*, 1155-1165.

51 T. Kircher, H. G. Löhmannsröben, *Phys. Chem. Chem. Phys.* **1999**, *1*, 3987-3992.

52 Y. Zhang, Z. Xu, L. Cai, G. Lai, H. Qiu, Y. Shen, *J. Photochem. Photobiol. A: Chem.* **2008**, *200*, 334-345.

53 W. W. Yu, L. Qu, W. Guo, X. Peng, *Chem. Mater.* **2003**, *15*, 2854-2860.

54 (a) J. Aldana, Y. A. Wang, X. Peng, *J. Am. Chem. Soc.* **2001**, *123*, 8844-8850. (b) M. Green, *J. Mater. Chem.* **2010**, *20*, 5797-5809. (c) A. M. Munro, D. S. Ginger, *Nano Lett.* **2008**, *8*, 2585-2590.

55 (a) J. Aguilera-Sigalat, S. Rocton, J. F. Sánchez-Royo, R. E. Galian, J. Pérez-Prieto, *RSC Adv.* **2012**, *2*, 1632-1638. (b) Z. Xie, T. Z. markus, G. Gotesman, Z. Deutsch, D. Oron, R. Naaman, *ACS Nano* **2011**, *5*, 863-869.

56 (a) J.Chen, J. L. Song, X. W. Sun, W. Q. Deng, C. Y. Jiang, W. Lei, J. H. Huang, R. S. Liu, *Appl. Phys. Lett.* **2009**, *94*, 153115-153118. (b) J-J. Park, P. Prabhakaran, K. K. Jang, Y. Lee, J. Lee, K. Lee, J. Hur, J-M. Kim, N. Cho, Y. Son, D-Y. Yang, K-S. Lee, *Nano Lett.* **2010**, *10*, 2310-2317.

57 S. Jeong, M. Achermann, J. Nanda, S. Ivanov, V. I. Klimov, J. A. Hollingsworth, *J. Am. Chem. Soc.* **2005**, *127*, 10126-10127.

58 J. Garcia-Hartjes, J. Dommerholt, T. Wennekes, F. L. van Delft, H. Zuilhof, *Eur. J. Org. Chem.* **2013**, 3712-3720.

59 B. R. Fisher, H. J. Eisler, N. E. Stott, M. G. Bawendi, *J. Phys. Chem. B* **2004**, *108*, 143-148.

[60] M. Jones, J. Nedeljkovic, R. J. Elingson, A. J. Nozik, G. Rumbles, *J. Phys. Chem. B* **2003**, *107*, 11346-11352.

[61] G-W. Shu, W-Z. Lee, I.-J. Shu, J-L. Shen, J. C-A. Lin, W. H. Chang, R-C. Ruaan, W. C. Chuo, *IEEE T. Nanotech.* **2005**, *4*, 632-636.